Practical analytical backscatter error bars for elastic one-component lidar inversion algorithm

Francesc Rocadenbosch,[1,2,*] M. Nadzri Md. Reba,[1,2]
Michaël Sicard,[1,2] and Adolfo Comerón[1]

[1]Remote Sensing Laboratory (RSLAB), Department of Signal Theory and Communications, Universitat Politècnica de Catalunya, Campus Nord, Jordi Girona 1-3, 08034 Barcelona, Spain (http://www.tsc.upc.edu/rslab)

[2]Institute for Space Studies of Catalonia–Aeronautics and Space Research Center, Universitat Politècnica de Catalunya, Barcelona, Spain

*Corresponding author: roca@tsc.upc.edu

Received 28 January 2010; revised 26 April 2010; accepted 27 April 2010;
posted 4 May 2010 (Doc. ID 123477); published 8 June 2010

We present an analytical formulation to compute the total-backscatter range-dependent error bars from the well-known Klett's elastic-lidar inversion algorithm. A combined error-propagation and statistical formulation approach is used to assess inversion errors in response to the following error sources: observation noise (i.e., signal-to-noise ratio) in the reception channel, the user's uncertainty in the backscatter calibration, and in the (range-dependent) total extinction-to-backscatter ratio provided. The method is validated using a Monte Carlo procedure, where the error bars are computed by inversion of a large population of noisy generated lidar signals, for total optical depths $\tau \leq 5$ and typical user uncertainties, all of which yield a practical tool to compute the sought-after error bars. © 2010 Optical Society of America

OCIS codes: 010.0010, 010.1290, 010.3640.

1. Introduction

Ground-based elastic backscatter lidars are still the most frequent type of lidar systems used, so far, in atmospheric aerosol remote sensing and play an essential role in "ground truth" calibration/validation [1] in support of space missions such as the Cloud Aerosol Lidar and Infrared Pathfinder Satellite Observation (CALIPSO, NASA-Centre National d'Études Spatiales) [2] and the Atmospherics Dynamics Mission (Atmospheric Dynamics Mission-AEOLUS, European Space Administration [3,4]). Cooperation between terrestrial lidar networks and satellite-borne lidars require of quality assured procedures both at the system and algorithm levels. The latter implies not only harmonizing the inversion procedures, but also providing error bar estimates along with the inverted optical parameters, which in turn (and when combined with multiwavelength lidar data) will be the subsequent input in the calculus chain to invert aerosol microphysical (size distribution) properties [5].

Backscatter lidars allow trustworthy derivation of the attenuated backscatter coefficient. Departing from previous results in the state of the art initiated as early as 1954 by Hitschfeld and Bordan [6] to invert the rain rate from radar returns and restated later to invert lidar returns by, e.g., Barrett and Ben-Dov [7], Viezee *et al.* [8], Davis [9], Fernald *et al.* [10], Collis and Russell [11], and Kohl [12], in 1981 Klett presented a stable backward method to invert the elastic single-scattering lidar equation using a one-component atmospheric model [13]. Later on, in 1984, Fernald presented a two-component inversion algorithm [14] (see also Ref. [15] and Section 4 in Ref. [16]), which is not studied here. The term "one-component" stands for no separation between molecular and aerosol components or, equivalently, for a "total" (aerosol plus molecular) optical component inversion method.

0003-6935/10/173380-14$15.00/0

Because the elastic-lidar equation is inherently undetermined for it contains two unknowns (the total atmospheric extinction and the total backscatter) and a proportionality constant representing the system constant, Klett's method requires two critical inputs from the user side: (i) a point backscatter calibration at a reference range (i.e., a range interval where the aerosol backscatter coefficient is negligible in front of the known molecular one) and (ii) provision of the total lidar ratio, which is defined as the (range-dependent) total-extinction-to-total-backscatter ratio.

Though, historically, Klett's method was formulated in total extinction terms [see Eqs. (11) [16]], trustworthy extinction profiles are hard to achieve [17–19]. This is because the extinction profile must be determined from the inverted backscatter-coefficient profile by multiplying the backscatter profile with the total lidar-ratio profile used before as input in the backscatter retrieval (following [17], typical extinction errors can be a factor five over backscatter errors). Therefore, when Klett's method is used to invert ground-based backscatter lidars without cooperative Raman channels or a scanning feature (these techniques enable independent inversion of extinction and backscatter profiles; see [20] for the elastic/Raman channel combination, and [21] for the scanning feature along with the assumption of a homogeneously horizontally stratified atmosphere), the method is usually employed in backscatter form.

Relevant Klett's variants and alternative methods are given in [22–24]. Thus, in [22] Kunz replaces the single-point calibration by a transmission loss calibration over the path of interest.

Concerning the impact of the uncertainties in the assumed user inputs to Klett's one-component inversion algorithm, several authors have studied its sensitivity to the boundary calibration [25–28] and to the total lidar-ratio [25,26]. Specifically, Qiu [27] provides error plots of the relative error on the retrieved optical thickness versus the relative boundary extinction calibration error parameterized for different atmospheric optical depths and forward/backward implementations of the method. Matsumoto and Takeuchi [28] provide a unified error approach (one- and two-component versions) in terms of an ad hoc normalized extinction and normalized range-dependent inversion error and give conclusions for different optically thick atmospheres using slant and sinusoidally modulated model optical paths.

Though, today, Fernald's two-component algorithm is the traditional way to retrieve the aerosol backscatter coefficient from elastic-lidar signals, Klett's one-component algorithm provides a similar but simpler numerical kernel [16], Eq. (22), to study the impact and error propagation of the different noise and user-uncertainty sources involved in explicit form. The utility of the one-component algorithm increases with increasing optical depth, so that for optical depths greater than approximately unity, the inversion method can be applied, in principle, using only information contained in the signal itself (i.e., with less sensitivity to misassessed user inputs) [13,29]. Besides, most 1064 nm problems (because of the lower molecular component in the near infrared, λ^{-4}-wavelength dependency) and 532 nm problems (for optically thick atmospheres) reduce to the one-component case. In fact, Klett's one-component and Fernald's two-component algorithms are mathematically equivalent in terms of the optical components retrieved, though by using different numerical kernels (Klett's uses "total" components and a range-dependent "total" lidar-ratio profile, while Fernald's uses "separated" aerosol/molecular components and an aerosol lidar-ratio profile). This motivates that the numerical sensitivity conclusions presented in this paper can be extrapolated to the two-component algorithm in a qualitative way.

Regarding the impact of noise, the Remote Sensing Laboratory (RSLAB) at the Universitat Polytechnica de Catalunya has recently first carried out a statistical-mathematical study to formally examine the way noise disturbs the inverted backscatter coefficient in the modern implementation of the one-component backward algorithm [30] (and on the two-component algorithm in [31]). A main conclusion is the bias effect, due to the noise affecting the calibration cell and propagating to all inversion cells. Further discussion on the one-component algorithm is found in [32–35].

In spite of these contributions above (with nearly all of them centered on the 1980s extinction retrieval form of the one-component algorithm rather than on its backscatter form), present-day elastic-lidar inversion still lacks a practical, systematic, and unified analytical formulation relating, in explicit form, the backscatter error bars (output) as a function of —and merging into a single body—all three error-sources involved (inputs): (i) errors due to the backscatter calibration, (ii) errors due to a misassessed range-dependent total lidar ratio, and (iii) errors due to the noise [range-dependent signal-to-noise ratio (SNR)]. Complementary, approximate limits of validity for such an analytical error-formulation are needed in terms of the SNR in the elastic-lidar channel, for this is a measurable "user" parameter. So far, RSLAB contributions [30,31] have covered (iii) in a mathematical-statistical way but are lacking the desired explicit (input-output) formulation. This is the objective of this paper. Thus, this paper leaves out physical discussion of the error bars obtained in terms of, e.g., the atmospheric optical depth, wavelength, or the physical correctness of the algorithm user inputs, for these topics have been discussed at length in the above references.

In Section 2, Klett's one-component method is revised and reformulated in a discrete vector function form. Section 3 is devoted to the mathematics of the derivation of the analytical error bars encompassing the above-mentioned error sources [concerning the error source (ii), a second-order formulation is presented for both range-dependent correlated and

uncorrelated lidar-ratio errors; concerning (iii)—and in contrast to [30]—a perturbational formulation is given]. In Section 4, the analytical error bars derived are cross examined with a Monte Carlo (MC) method, and in Section 5, concluding remarks are given.

2. Review of Klett's One-Component Inversion Method

A. Review of Klett's Backward Method

The single-scattering monochromatic pulsed elastic-lidar equation is formulated as

$$P(R) = \frac{A}{R^2}\beta(R)\exp\left[-2\int_0^R \alpha(r)\mathrm{d}r\right]\xi(R), \qquad (1)$$

where $P(R)$ is the background-corrected power received from range R (at the photodetector plane) at the emission wavelength λ, $\alpha(R)$ and $\beta(R)$ are the total atmospheric extinction and backscatter coefficients, respectively, and A is the instrument system constant [$A = EA_r\xi(\lambda)c/2$, with E being the emitted pulse energy, A_r the effective telescope receiving area, $\xi(\lambda)$ the optics net transmissivity, and c the speed of light]. The term $\xi(R)$ represents the normalized crossover function between the telescope field of view and the laser beam and is assumed to be unity (alternatively, it is assumed to be known from geometrical optics [11]) in the inversion range of interest, an important prerequisite for proper inversion in the near-range [17], though not studied here.

Klett's one-component inversion solution [13] in total-backscatter form (KLT for short in what follows) is reformulated as

$$\beta(R) = \frac{\beta_m[R^2P(R)]}{[R_m^2P(R_m)] + 2\beta_m\int_R^{R_m} S(r)[r^2P(r)]\mathrm{d}r}, \qquad (2)$$

where $\beta_m = \beta(R_m)$ is the total backscatter calibration at the calibration range R_m, $S(R)$ is the total extinction-to-backscatter lidar ratio ($S(R) = \alpha(R)/\beta(R)$, in what follows, the "total lidar ratio"), and the remaining variables have already been defined in Eq. (1). Equation (2) is a close reformulation of Eq. 9 in [9] and Eq. 22 in [16].

If the calibration point is given at the far end of the inversion range (i.e., $R \le R_m$), Eq. (2) represents the "backward form." Conversely, if the calibration point is given at the near end (i.e., $R \ge R_m$), Eq. (2) represents the "forward form," and, consequently, Eq. (2) must have integration limits from R_m to R and a minus sign preceding the integration sign [13,25]. In practice, a midrange calibration is often used, which involves backward and forward integration from that point, therefore covering the full inversion range of interest (see Section 4B in [27] for a discussion on the stability as a function of the optical thickness).

B. Modified Backward Discrete Klett's One-Component Inversion Solution in Total-Backscatter Form

Introducing the range-corrected power, $U(R)$, and the cumulative integral of the range-corrected power times the total lidar ratio, $G(R)$, as the auxiliary functions

$$\begin{cases} U(R) = R^2P(R) \\ G(R) = \int_R^{R_m} S(r)U(r)\mathrm{d}r \end{cases}, \qquad (3)$$

and the discrete range $R_j = R_{\min} + (j-1)\Delta R$, $j = 1\ldots N$ with ΔR the spatial resolution of the lidar data to be inverted, Eq. (2) can be rewritten as

$$\beta_j(\beta_N, \vec{S}, \vec{U}) = \frac{\beta_N U_j}{U_N + 2\beta_N G_j(\vec{S}, \vec{U})}, \qquad (4)$$

where U_j and G_j stand, respectively, for $U(R_j)$ and $G(R_j)$. Notation $\beta_j(\beta_N, \vec{S}, \vec{U})$ is a reminder that the total inverted backscatter at range cell $R = R_j$ depends on the backscatter user calibration at the far range, $\beta_N = \beta(R_N)$, the user-input lidar ratio, $\vec{S}$ (i.e., the function $S(R)$ in vector form), and the range-corrected power, $\vec{U}$ (i.e., the function $U(R)$ in vector form). Similarly, $G_j(\vec{S}, \vec{U})$ is a reminder that the integral function $G_j = G(R_j)$ has explicit dependency on the lidar ratio, $\vec{S}$, and on the range-corrected power, $\vec{U}$, via Eq. (3).

We now see that, irrespective of the numerical integration method used, G_j is always computed in Eq. (3) as a linear combination of N uniformly spaced points with appropriate weights w_i as

$$\begin{cases} G_j = \sum_{i=j}^N w_i S_i U_i & j < N \\ G_N = 0 & j = N \end{cases}. \qquad (5)$$

For example, in the case of rectangle integration and $N \ge 2$ points, the integration weights are $w_i = h$, $i = 1\ldots N-1$; $w_N = 0$ with $h = \Delta R$ being the integration step. Likewise, in the case of trapezium integration ($N \ge 3$), $w_i = h/2$ $i = 1, N$; $w_i = h$, $i = 2\ldots N-1$.

C. Modified Forward Discrete Klett's One-Component Inversion Solution in Total-Backscatter Form

In the forward form of the one-component algorithm, the following changes must be introduced:

1. The far-range calibration at $R = R_N$ must be replaced by the near-range calibration $R = R_1$ (i.e., $\beta_N \to \beta_1$) in Eq. (4).
2. Equation (4) has a minus sign as follows:

$$\beta_j(\beta_1, \vec{S}, \vec{U}) = \frac{\beta_1 U_j}{U_1 - 2\beta_1 G_j(\vec{S}, \vec{U})}. \qquad (6)$$

3. Equation (5) is computed from $i = 1$ to j [$\sum_{i=1}^j(.)$ instead of $\sum_{i=j}^N(.)$].
4. Consequently, the "smaller than" sign ($<$) must be replaced by a "greater than" sign ($>$), and "$\ge$" by "$\le$" in subsequent inequalities.

3. Total-Backscatter Analytical Error Bars

In what follows, we consider the backward case only. It is a straightforward task to derive the forward case using Subsection 2.C remarks.

A. Overview: Error-Propagation Approach

By revisiting Eq. (4), it is convenient to distinguish the following error sources influencing the total backscatter inverted: (i) the calibration error on the backscatter calibration, β_N, (ii) errors on the (user-proposed) range-dependent lidar ratio, $\vec{S}$, (iii) the noise corrupting the return power (equivalently, the range-corrected power vector $\vec{U}$) in all range cells except at the calibration cell, and (iv) the noise corrupting the return power at the calibration cell. This "fictitious" division between error sources (iii and iv) accounts for the fact that in practical lidar inversion, it is customary to minimize the return-power noise at the calibration point by spatially averaging (e.g., rectangular smoothing window) a few power samples around that point. As a result, the SNR at the calibration cell is substantially higher than that of its neighbor cells. The significance of noise in the calibration term was historically outlined in [32], and the noise-reduction advantages of this technique have also been illustrated in [30]. In what follows, this division is retained for methodological reasons.

Before proceeding further, we note that while the error source (i) is rooted at the far-range calibration cell, $R = R_N$, error sources (ii, iii, and iv) arise from each individual inversion cell, R_j, and propagate inversion errors down to all inversion cells.

In order to study the behavior of the error-propagated backscatter error, and just as a first step towards computation of the total-backscatter error bars, we apply classic error-propagation laws to Eq. (4) as follows:

$$\begin{cases} |d\beta_j| = \left|\frac{\partial\beta_j}{\partial\beta_N}d\beta_N\right| + \sum_{k=1}^{N}\left|\frac{\partial\beta_j}{\partial S_k}dS_k\right| + \sum_{k=1}^{N-1}\left|\frac{\partial\beta_j}{\partial P_k}dP_k\right| + \left|\frac{\partial\beta_j}{\partial P_N}dP_N\right|; & j < N \\ |d\beta_j| = |d\beta_N|; j = N \end{cases}, \tag{7}$$

where for the case $j < N$ we define

$$\varepsilon_{j,1} = \frac{\partial\beta_j}{\partial\beta_N}d\beta_N = \left(\frac{\beta_j}{\beta_N}\right)^2\frac{U_N}{U_j}d\beta_N, \tag{8}$$

$$\varepsilon_{j,2} = \sum_{k=1}^{N}\frac{\partial\beta_j}{\partial S_k}dS_k = -\frac{2\beta_j^2}{U_j}\sum_{k=j}^{N}w_kU_kdS_k, \tag{9}$$

$$\varepsilon_{j,3} = \sum_{k=1}^{N-1}\frac{\partial\beta_j}{\partial P_k}dP_k = \frac{\beta_j}{U_j}dU_j - \frac{2\beta_j^2}{U_j}\sum_{k=j}^{N}w_kS_kdU_k, \tag{10}$$

$$\varepsilon_{j,4} = \frac{\partial\beta_j}{\partial P_N}dP_N = -\frac{\beta_j^2}{\beta_NU_j}dU_N - \frac{2\beta_j^2}{U_j}w_NS_NdU_N \approx -\frac{\beta_j^2}{\beta_NU_j}dU_N, \tag{11}$$

where $d\beta_N$, dS_k, dP_k, and dP_N, respectively, represent the error sources (i–iv) described above (see Appendix A for mathematical details). Equation (11) can directly be approximated by $\varepsilon_{j,4} \approx -(\beta_j^2/\beta_NU_j) \times dU_N$, for the ratio between the second and the first term on the right member of this equation becomes $|2w_NS_N\beta_N| \ll 1$ [it can be shown that $|2w_NS_N\beta_N|$ is typically between 6×10^{-3} and 6×10^{-6} for typical total lidar ratios in the 10–100 sr range [36], β_N in the molecular range, and ranging from 2.8×10^{-6} m^{-1} sr^{-1} (355 nm, 10 km height) to 3.2×10^{-8} m^{-1} sr^{-1} (1064 nm, 10 km height), and $w_N \approx 10$ m (a typical inversion resolution)].

The error-propagated backscatter error for the case $j = N$ in Eq. (7) is directly the backscatter-calibration error at the calibration cell, $d\beta_j = d\beta_N$; $j = N$; see Eqs. (2) and (3). Recall that because the backscatter calibration at the far range is a user input to the algorithm, the assumed calibration error, $d\beta_N$, must be assessed from the user's side.

The next step to compute the total-backscatter error is to interpret $d\beta_N$, dS_k, and $dP_k (k = 1 \ldots N)$ [note that $dU_k = R_k^2 dP_k$ after Eq. (3)] as equivalent Gaussian random variables with standard deviations σ_{β_N}, σ_{S_k}, and $\sigma_{n_k} (k = 1 \ldots N)$, respectively. σ_{β_N} and σ_{S_k}, respectively, express the user's uncertainty as the $1-\sigma$ standard deviation on the user-input backscatter calibration, β_N, and user-input range-dependent total lidar ratio, $S_k = S(R_k)$. σ_{n_k} models the range-dependent noise standard deviation at each range cell $R = R_k$. In practice, for lidar systems operating in shot-dominant mode (Poisson statistics), σ_{n_k} can simply be estimated as the square root of the signal component. The Gaussian approximation is justified on account of the fact that for count rates above approximately 50, the Poisson probability density function looks very much like a Gaussian [37]. In the more general case corresponding to modest-energy small-aperture lidar systems where the noise-dominant regime changes along the observation range of interest (e.g., from shot dominant in the near range to Gaussian dominant at the far range and mixed-mode in between), the range-dependent noise standard deviation, σ_{n_k}, can be estimated by a piecewise approach in which the

standard deviation is computed over small adjacent subintervals along the lidar range or using more advanced discrete-time SNR estimators [38].

B. Computation: Stochastic Approach

Departing from $d\beta_N$, dS_k, and $dP_k(k=1\ldots N)$ as independent Gaussian random variables with variances σ_{β_N}, σ_{S_k}, and σ_{n_k}, the total-backscatter error of Eq. (7) at each cell $R=R_j$ is computed as the error of standard deviation

$$\sigma_{\beta j}=\begin{cases}\left(\sigma^2_{\varepsilon_{j,1}}+\sigma^2_{\varepsilon_{j,2}}+\sigma^2_{\varepsilon_{j,3}}+\sigma^2_{\varepsilon_{j,4}}\right)^{\frac{1}{2}}, & j<N\\ \sigma_{\beta N}, & j=N\end{cases}, \tag{12}$$

where the terms $\sigma^2_{\varepsilon_{j,1-4}}$ are computed after Eqs. (8)–(11) in Subsections 3.B.1, 3.B.2, 3.B.3, and 3.B.4 next.

1. *Error Due to Backscatter Calibration, $\sigma_{\varepsilon_{j,1}}$*

From Eq. (8) it is straightforward calculus that

$$\sigma_{\varepsilon_{j,1}}=\left|\left(\frac{\beta_j}{\beta_N}\right)^2\frac{U_N}{U_j}\right|\sigma_{\beta_N}. \tag{13}$$

Equation (13) expresses that errors on the backscatter calibration propagate downrange to all inversion cells.

2. *Error Due to (Range-Dependent) Lidar Ratio, $\sigma_{\varepsilon_{j,2}}$*

Here we consider two subcases:

Correlated Lidar-Ratio Errors with Range

This is the most sensible case, for it assumes that errors on the user-input lidar ratio can be expressed in terms of a user-estimated systematic relative error p from the true atmospheric lidar ratio:

$$dS(R)=pS(R)\Leftrightarrow dS_k=pS_k. \tag{14}$$

Consequently, the "true" lidar ratio is assumed to lie between $S(R)(1\pm p)$ at $1-\sigma$ confidence level. Substituting Eq. (14) into Eq. (9) and using Eq. (5) yields

$$\sigma_{\varepsilon_{j,2}}=\left|p\frac{2\beta_j^2}{U_j}G_j\right|. \tag{15}$$

A second-order expansion of Eq. (4) around p [in contrast to the first-order expansion of Eq. (7), see Appendix B for mathematical details] is given by

$$\sigma'_{\varepsilon_{j,2}}=\left|\pm p\frac{2\beta_j^2}{U_j}G_j+p^2\frac{4\beta_j^3}{U_j^2}G_j^2\right|. \tag{16}$$

Practical experiment under the simulation conditions of Subsection 4.C and $p=10\%$ has shown that the second-order term of Eq. (16) can contribute up to 18% of the total figure of $\sigma'_{\varepsilon_{j,2}}$. Besides, a major advantage is that the $\pm$ sign gives nonsymmetrical error bars, particularly for large values of p (the "+" and "–" signs corresponding to the upper and lower error bars, respectively), all of which recommends second-order expansion.

Uncorrelated Lidar-Ratio Errors with Range

This assumes the questionable hypothesis (further discussion in Subsection 4.C) that lidar-ratio errors between any two different range cells are statistically uncorrelated. Formally, that

$$E[dS_i dS_j]=0 \qquad i\neq j. \tag{17}$$

In particular, Eq. (17) means that lidar-ratio errors (dS_i, dS_j) over relatively close or adjacent range cells are completely different random realizations and that, therefore, they can average out when integrated over the inversion path. This case may correspond to the situation in which the lidar-ratio profile along with pertinent noise-induced error bars (to be assimilated into S_k and dS_k, respectively) is known, for example, from an elastic/Raman lidar system, in which case the one-component inversion algorithm is used to validate the backscatter profile formerly obtained by such an elastic/Raman instrument. Otherwise, the present case in this section is unlikely and can only be accepted as a lower error bound for comparison with the correlated case above.

To compute the backscatter-propagated error, $\sigma_{\varepsilon_{j,2}}$, we interpret the discrete integral term of Eq. (9):

$$I_j^{GS}=\sum_{k=j}^{N}w_kU_kdS_k, \tag{18}$$

as a linear combination of random Gaussian variables dS_k [with user-defined variances equal to $\sigma^2_{S_k}(k=1\ldots N)$] weighted by $c_k=w_kU_k$. Superscript "GS" in Eq. (18) is a reminder that the discrete summation is formally identical to the definition of G_j in Eq. (5), except for the fact that the lidar ratio, S_i, has been replaced now by its error, dS_i. From Eqs. (17) and (18) above, it follows that

$$\sigma^2_{GS,j}=\sum_{k=j}^{N}c_k^2\sigma^2_{S_k}=\sum_{k=j}^{N}(w_kU_k)^2\sigma^2_{S_k}. \tag{19}$$

Finally, by reintroducing Eqs. (18) and (19) into Eq. (9), the sought-after (uncorrelated) error due to a (range-dependent) total lidar ratio becomes

$$\sigma_{\varepsilon_{j,2}}=\left|\frac{2\beta_j^2}{U_j}\right|\sigma_{GS,j}. \tag{20}$$

3. *Error Due to Observation Noise (Range Cells 1…N – 1), $\sigma_{\varepsilon_{j,3}}$*

Additive noise to the "ideal" (i.e., noiseless) lidar return power of Eq. (1) can be assumed an equivalent range-independent Gaussian noise; see Subsection 3.A. Thus, if dP_j is the power fluctuation due to noise, then dP_i and $dP_j (i \neq j)$ are uncorrelated random variables. Formally,

$$E[dP_i dP_j] = 0 \qquad i \neq j. \tag{21}$$

For mathematical convenience, we reintroduce the range-corrected power, $U_j = R_j^2 P_j$ of Eq. (3), and its related range-corrected error, $dU_j = R_j^2 dP_j$, as our primary variables. From this basis, computation of the error due to the observation noise, $\sigma_{\varepsilon_{j,3}}$, parallels the methodology of Subsection 3.B.2 above. By defining the discrete integral term of Eq. (10)

$$I_j^{GU} = \sum_{k=j}^{N} w_k S_k dU_k, \tag{22}$$

its variance is computed as

$$\sigma_{GU,j}^2 = \sum_{k=j}^{N} (w_k S_k)^2 \sigma_{U_k}^2. \tag{23}$$

Finally, the error due to the observation noise becomes

$$\sigma_{\varepsilon_{j,3}} = \left[\left(\frac{\beta_j}{U_j} \right)^2 \sigma_{U_j}^2 + \left(\frac{2\beta_j^2}{U_j} \right)^2 \sigma_{GU,j}^2 \right]^{\frac{1}{2}}. \tag{24}$$

The inverse of the SNR:

$$\mathrm{SNR}_j = \frac{U_j}{\sigma_{U_j}}, \tag{25}$$

is clearly identified in the first term of Eq. (24).

4. *Error Due to Observation Noise at Calibration Cell (Range Cell N), $\sigma_{\varepsilon_{j,4}}$*

From Eq. (11) above, we have

$$\sigma_{\varepsilon_{j,4}} = \left(\left| \frac{\beta_j^2}{\beta_N U_j} \right| + \left| \frac{2\beta_j^2}{U_j} w_N S_N \right| \right) \sigma_{U_N} \approx \left| \frac{\beta_j^2}{\beta_N U_j} \right| \sigma_{U_N}, \tag{26}$$

where σ_{U_N} is the standard deviation associated to the range-corrected noise random variable at the calibration cell $dU_N = R_N^2 dP_N$, i.e., $\sigma_{U_N} = R_N^2 \sigma_{n_N}$.

4. Discussion Examples

In order to validate the analytical approach presented in Subsection 3.B, the analytical error bars derived so far must be compared with the true ones obtained from an MC simulation method. In the MC method, a large set of noisy backscatter profiles are inverted in response to synthetically generated noisy lidar returns and compared with the input (noiseless) atmospheric backscatter used to generate them (at this point, note that live data cannot serve the purpose, for the true atmospheric backscatter profile must be known). As a result, the inversion error committed is obtained.

The simulation scenario considered is illustrated in Fig. 1, where a set of 100 independent noisy elastic-lidar returns at 532 nm wavelength has been stochastically generated [see range-corrected power in Fig. 1(b)] in response to the synthetic atmosphere and range-dependent SNR (SNR) of Figs. 1(a) and 1(b), respectively. To make the scene fully realistic, a two-component atmosphere has been generated by combining a United States standard atmosphere molecular model [39] (boundary conditions are 15 °C and 1013.15 hPa at ground level) with an atmospheric aerosol component, where the aerosol backscatter has been digitally interpolated (down to the spatial resolution of the simulation, $\Delta R = 7.5$ m) from a real

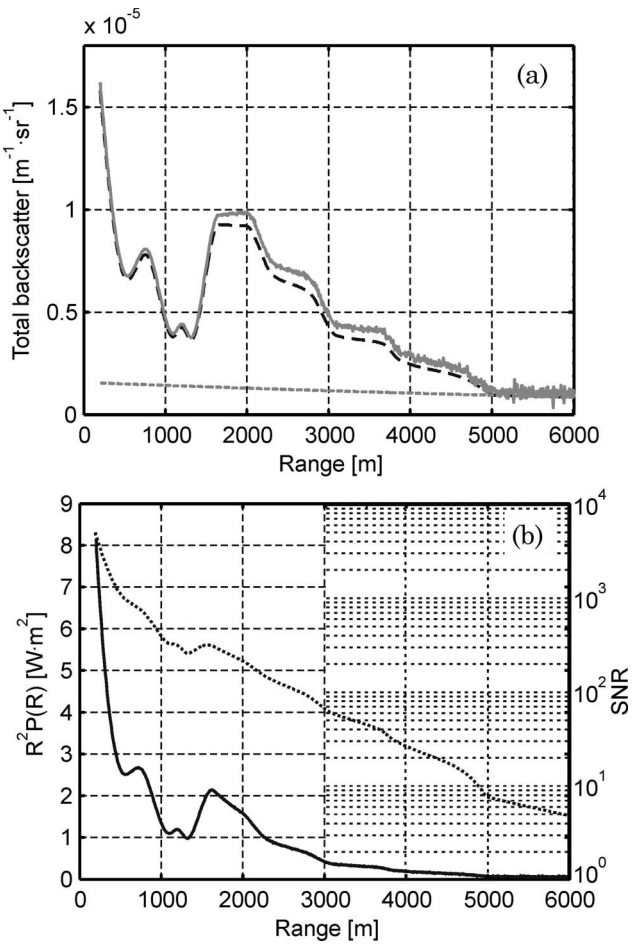

Fig. 1. Simulation scenario at 532 nm wavelength (R is the slant path distance, elevation angle 54 °, sounding range 0.2 to 6 km): (a) atmospheric backscatter components: (dashed black) noiseless total backscatter used as the simulation input, (solid gray) example of a noise-corrupted inverted backscatter representative, and (dashed gray) Rayleigh backscatter component and (b) (solid trace) range-corrected return power after 1 s integration time, (dotted trace) SNR [$\mathrm{SNR}(R_{\min}) = 5 \times 10^3$ and $\mathrm{SNR}(R_{\max}) = 5$].

measurement obtained at an elevation angle of 54 ° with the elastic-Raman lidar instrument of the RSLAB in the framework of the European Aerosol Research Lidar Network (EARLINET) regular measurements. An aerosol lidar ratio of $S^{\mathrm{aer}} = 50$ sr has been assumed.

At this point, and in connection with Eq. (2), we recall that the one-component algorithm inverts the total-backscatter profile (i.e., molecular plus aerosol components) given a (noisy) lidar return, a (user-input) backscatter calibration, and a (user-input) total lidar ratio profile. Therefore, the total backscatter and the total lidar ratio have been set as the key atmospheric quantities for the simulator [the former computed as $\beta(R) = \beta^{\mathrm{aer}}(R) + \beta^{\mathrm{mol}}(R)$; the latter computed as $S(R) = \alpha(R)/\beta(R)$, where $\alpha(R) = S^{\mathrm{aer}}(R) \times \beta^{\mathrm{aer}}(R) + \frac{8\pi}{3}\beta^{\mathrm{mol}}(R)$]. Formally,

$$S(R) = \frac{S^{\mathrm{aer}}(R)\beta^{\mathrm{aer}}(R) + \frac{8\pi}{3}\beta^{\mathrm{mol}}(R)}{\beta^{\mathrm{aer}}(R) + \beta^{\mathrm{mol}}(R)}. \tag{27}$$

This leads to a total lidar ratio between approximately 35–45 sr in the 0.2–3.8 km range and a monotonically decreasing total lidar ratio from approximately 35 sr down to $S_{\mathrm{mol}} = 8\pi/3$ (the molecular ratio) in the 3.8–5 km range. From 5 km onwards, the scattering is purely molecular. The simulated atmospheric total optical depth ($\tau = \int_0^{R_{\max}} [\alpha^{\mathrm{aer}}(r) + \alpha^{\mathrm{mol}}(r)]\mathrm{d}r$) is $\tau \approx 1.2$, corresponding to an approximate mean visibility of 20 km.

System parameters are based on the RSLAB lidar instrument {160 mJ energy, 532 nm wavelength, 6 ns pulse width, frequency-doubled Nd:YAG laser; 20 cm aperture, 2 m focal-length telescope; 3 mm, 56% quantum-efficiency avalanche photodiode; and receiving channel NEP $= 4.2 \times 10^{-13}[W \cdot \mathrm{Hz}^{-1/2}]$—NEP stands for noise equivalent power}. The receiver channel noise is modeled using a range-dependent noise equivalent variance merging into a single-body signal-shot photoinduced, dark-shot, and thermal Gaussian noise contributions (a complete model is given in Ref. [29], Appendix A). The SNR at the starting range of inversion, $R_{\min} = 0.2$ km (full laser-telescope overlap), is as high as 5×10^3 and progressively decreases to a modest figure of 5 at the maximum range of inversion, $R_{\max} = 6$ km.

The calibration range is chosen coincident with the maximum inversion range, $R_{\mathrm{cal}} = R_{\max} = 6$ km, where the total backscatter ($\beta_N = \beta_N^{\mathrm{mol}} + \beta_N^{\mathrm{aer}}$) falls into the molecular level, so that $\beta_N^{\mathrm{aer}} \ll \beta_N^{\mathrm{mol}}$ and, consequently, $\beta_N \approx \beta_N^{\mathrm{mol}} = 1.1 \times 10^{-6}\ \mathrm{m}^{-1}\ \mathrm{sr}^{-1}$. The boundary layer ends at approximately 5 km along the range.

The discussion examples presented next address the four error sources studied in Subsections 3.B.1, 3.B.2, 3.B.3, and 3.B.4., which are now revisited in altered order for illustrative purposes. When computing the total-backscatter error bars, summary Table 1 has been used, and—as happens with real measurements—variables U_j and β_j have been replaced by their noisy estimates (i.e., the range-corrected lidar return power in the case of U_j and the noisy inverted backscatter in the case of β_j).

A. Effects of Range-Dependent Signal-to-Noise Ratio

1. Noise Corrupting Return Power in All Range Cells Except at Calibration Cell [Error Source (iii), $\sigma_{\varepsilon_{j,3}}$ in Table 1 and Subsection 3.B.3; see Fig. 2]

In accordance with the superposition principle, the simulation is carried out with SNR(R) following Fig. 1(b) for $R \neq R_{\mathrm{cal}}$ and all other error sources deactivated {i.e., no noise on the return power at

Table 1. Summary Table to Compute Total-Backscatter Analytical Error Bars in Klett's Backward Inversion Method Due to Error Sources (i–iv) in Subsection 3.B[a]

What Models	Formula	Reference
A. Total backscatter error bar (case $j < N$), where	$\sigma_{\beta j} = (\sigma^2_{\varepsilon_{j,1}} + \sigma^2_{\varepsilon_{j,2}} + \sigma^2_{\varepsilon_{j,3}} + \sigma^2_{\varepsilon_{j,4}})^{\frac{1}{2}}$	Equation (12)
(i) Error due to the backscatter calibration	$\sigma_{\varepsilon_{j,1}} = \left\lvert \left(\frac{\beta_j}{\beta_N}\right)^2 \frac{U_N}{U_j} \right\rvert \sigma_{\beta_N}$	Equation (13)
(ii) Error due to the (range-dependent) lidar ratio (correlated case)	$\sigma^C_{\varepsilon_{j,2}} = \left\lvert \pm p \frac{2\beta_j^2}{U_j} G_j + p^2 \frac{4\beta_j^3}{U_j^2} G_j^2 \right\rvert$	Equation (16)
where	$G_j = \sum_{i=j}^N w_i S_i U_i$	Equation (5)
(Uncorrelated case)	$\sigma_{\varepsilon_{j,2}} = \left\lvert \frac{2\beta_j^2}{U_j} \right\rvert \sigma_{GS,j}$	Equation (20)
where	$\sigma^2_{GS,j} = \sum_{k=j}^N (w_k U_k)^2 \sigma^2_{S_k}$	Equation (19)
(iii) Error due to the observation noise (range cells 1…N – 1)	$\sigma_{\varepsilon_{j,3}} = \left[\left(\frac{\beta_j}{U_j}\right)^2 \sigma^2_{U_j} + \left(\frac{2\beta_j^2}{U_j}\right)^2 \sigma^2_{GU,j} \right]^{\frac{1}{2}}$	Equation (24)
where	$\sigma^2_{GU,j} = \sum_{k=j}^N (w_k S_k)^2 \sigma^2_{U_k}$	Equation (23)
(iv) Error due to the observation noise at the calibration cell (range cell N)	$\sigma_{\varepsilon_{j,4}} = \left(\left\lvert \frac{\beta_j^2}{\beta_N U_j} \right\rvert + \left\lvert \frac{2\beta_j^2}{U_j} w_N S_N \right\rvert \right) \sigma_{U_N} \approx \left\lvert \frac{\beta_j^2}{\beta_N U_j} \right\rvert \sigma_{U_N}$	Equation (26)
B. Total backscatter error bar (case $j = N$, calibration point)	$\sigma_{\beta j} = \sigma_{\beta_N}$	

[a]Follow Subsection 2.C for the forward variant. Upper/lower error bar is +/− sign, respectively.

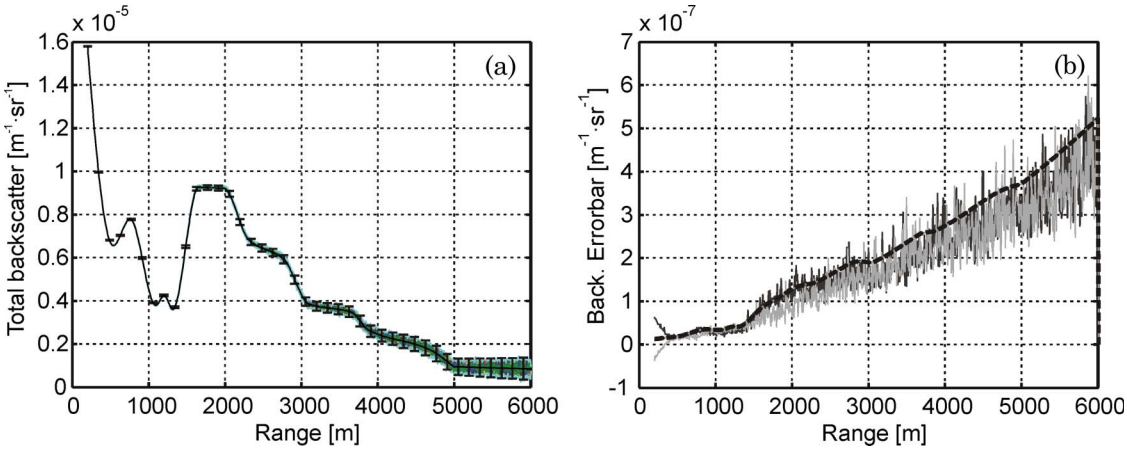

Fig. 2. (Color online) Error source (iii), $\sigma_{\varepsilon_{j,3}}$ (see Table 1 and Subsection 3.B.3): noise corrupting the return power in all range cells except at the calibration cell. (a) MC total backscatter inversion with superimposed $3-\sigma$ analytical error bars (vertical error bar lines). The set of 100 noise-corrupted lidar returns inverted in the MC method appears as a growing shadowed area from 2000 m onwards. (b) Comparison between the backscatter error bar amplitudes derived from both the MC and the analytical method as a function of range. Upper and lower MC backscatter error amplitudes are plotted in dark and light gray solid traces (noisy and nearly coincident), respectively. Analytical error bars are plotted in dark dashed traces for comparison.

the calibration cell, $\mathrm{SNR}(R_{\mathrm{cal}}) \to \infty$ [error source (iv)]; perfect backscatter calibration [error source (i)]; known total lidar ratio [error source (ii)]}.

Figures 2(a) and 2(b) plot the $3-\sigma$ analytical error bars for the total backscatter according to Eq. (24) in two different ways: in Fig. 2(a) the analytical error bars are plotted as vertical lines centered in the simulated atmospheric backscatter along with a family of $N = 100$ inverted backscatter profiles from the MC method. Excellent agreement results with virtually all inverted profiles inside the predicted analytical error bars. In Fig. 2(b) the amplitude of the $3-\sigma$ analytical backscatter error bars is compared with that of the MC error bars. While the analytical error bars are symmetric (first-order approximation for the present error source), i.e., with equally distributed upper and lower error amplitudes, the MC error bars are, in principle, not. Thus, while the error amplitude in Fig. 2(b) in the case of the analytical error bars is just equal to half the vertical error bar lines plotted in Fig. 2(a), we distinguish between the upper and lower error amplitudes in the case of MC error bars. The MC backscatter upper error amplitude (noisy dark gray solid curve) is the difference between the upper envelope of the family of inverted backscatter profiles in Fig. 2(a) and the atmospheric backscatter solution. Likewise, the lower error amplitude (noisy light gray solid curve) is the difference between the atmospheric backscatter solution and the lower family envelope.

As expected in response to a decreasing SNR with range, the effect of error source (iii) is progressively increasing error bars with range.

2. *Noise Corrupting Return Power at Calibration Cell [Error Source (iv), $\sigma_{\varepsilon_{j,4}}$ in Table 1 and Subsection 3.B.4; See Fig. 3]*

The SNR simulation conditions set for this error source are the dual case of Subsection 4.A.1 above,

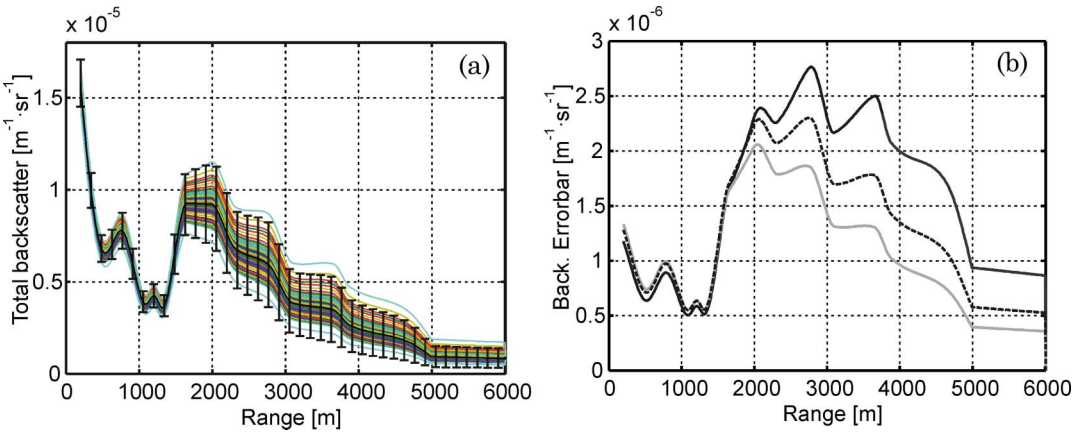

Fig. 3. (Color online) Error source (iv), $\sigma_{\varepsilon_{j,4}}$ (see Table 1 and Subsection 3.B.4): noise corrupting the return power at the calibration range [$\mathrm{SNR}(R_{\mathrm{cal}}) = 5$, $\mathrm{SNR}(R) \to \infty, R \neq R_{\mathrm{cal}}$]. (a)–(b)–Same descriptors as in Fig. 2. In contrast to Fig. 2, the noise effects due to this error source backpropagate to all inversion cells and become more important, as shown by a considerably large spread of the inverted backscatter family.

i.e., $\mathrm{SNR}(R) \to \infty$, $R \neq R_{\mathrm{cal}}$ and $\mathrm{SNR}(R_{\mathrm{cal}}) = 5$, all other error sources deactivated.

As seen in Fig. 3, the impact of a noisy power return at the calibration range propagates backward to the minimum inversion range and affects all inversion cells. In contrast to Subsection 4.A, the inversion error increases from the calibration cell downrange to approximately 1.6 km, inside the boundary layer, where the SNR has a comfortable value of 25 dB. Though the present simulation example corresponds to a relatively turbid atmosphere (one-way optical depth, $\tau \approx 1.2$), it is easy to show that for relatively clear atmospheres, the backscatter error behavior with range, $\sigma_{\varepsilon_{j,4}}$, tends to be proportional to the backscatter term, β_j. Thus, with reference to Eq. (26), the range-dependent behavior of $\sigma_{\varepsilon_{j,4}}$ is given by the ratio β_j^2/U_j, which for clear atmospheres [$U_j \approx A\beta_j$, Eq. (1)] is proportional to the backscatter term, β_j. For turbid atmospheres, as is the case, the behavior of U_j suffers the effect of a nonnegligible atmospheric transmittance dictated by the lidar Eq. (1); however, a reminiscence of the backscatter shape is still reencountered in Fig. 3(b) in the 1.6–6 km range.

Figure 3(b) shows that the backscatter error bars computed via the analytical error bars presented are in fairly good agreement with the MC error bars; the estimated analytical error falling in between the upper and lower MC error bars (upper and lower error bars are no longer coincident because of the comparatively higher backscatter errors; at 2 km the relative backscatter error is as high as 22%). By comparing Fig. 3(b) with Fig. 2(b) it arises that the noise corrupting the calibration cell is the dominant error source ahead of the noise due to all other range cells (i.e., $\sigma_{\varepsilon_{j,4}} > \sigma_{\varepsilon_{j,3}}$ for most of the inversion range). This is in accordance with previously published results [30], where, though lacking a practical methodology to compute the noise-induced backscatter error bars, it is emphasized the importance of enhancing the SNR at the calibration cell, $\mathrm{SNR}(R_{\mathrm{cal}})$, by spatially averaging the return power of neighboring cells.

3. *Superposition of Error Sources A1 and A2 ($\sigma_{\varepsilon_{j,3}}$ and $\sigma_{\varepsilon_{j,4}}$ in Table 1)*

Figures 4(a) and 4(b) show the effects of the range-dependent SNR of Fig. 1(b) (noise corrupting all cells) without that spatial averaging. Judging by Fig. 4(b), the dominance of the calibration-cell noise effects is evidenced by backscatter errors in Fig. 4(b) virtually

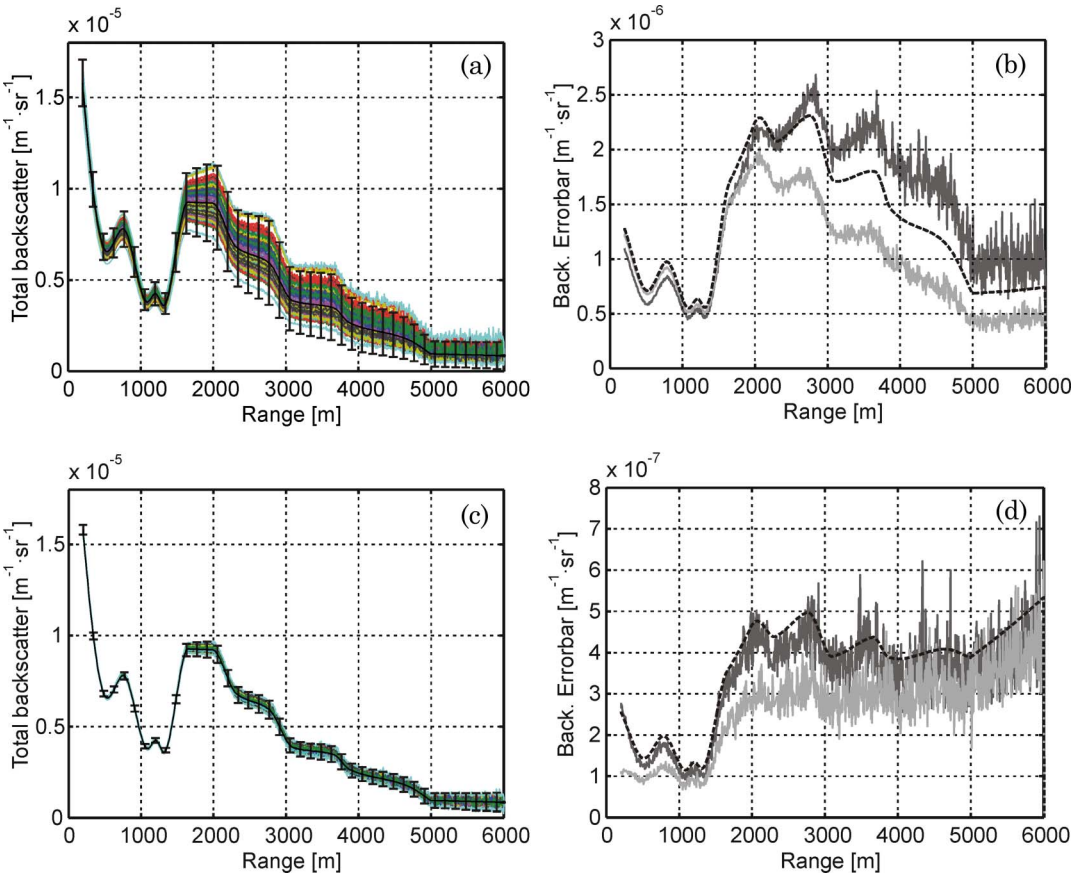

Fig. 4. (Color online) Counteracting noise in practical lidar inversion: corroboration of previously published results. Same descriptors as in Fig. 2 for subsets (a)–(b) and (c)–(d). Subset (a)–(b) corresponds to the superposition of error sources (3) and (4), $\sigma_{\varepsilon_{j,3}}$ and $\sigma_{\varepsilon_{j,4}}$ (see Subsections 3.B.3 and 3.B.4), which stands for noise corrupting *all* the cells along the data inversion range [SNR, as in Fig. 1(b)]. Simulation conditions for subset (c)–(d) are identical to (a)–(b) except that the SNR at the calibration range has been enhanced to $\mathrm{SNR}(R_{\mathrm{cal}})' = \mathrm{SNR}(R_{\mathrm{cal}})\sqrt{N} = 25$ by spatially averaging $N = 25$ neighbor return-power cells.

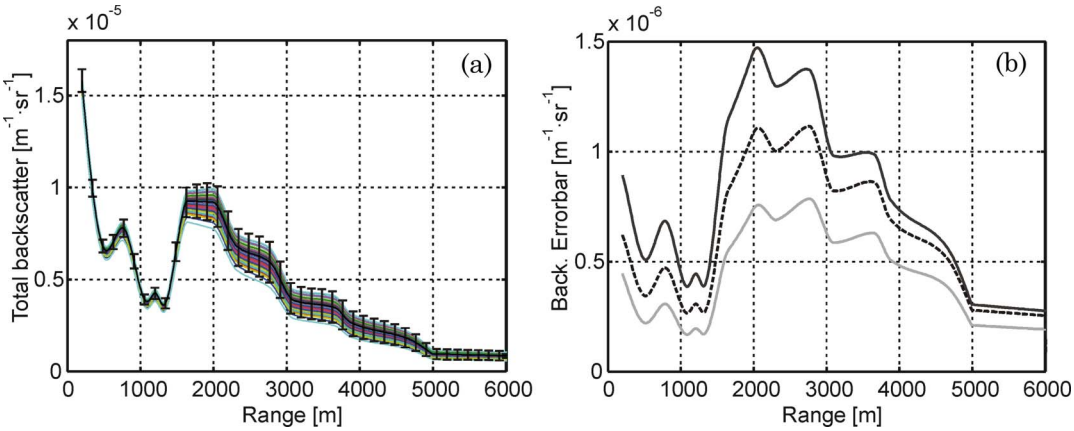

Fig. 5. (Color online) Error source (i), $\sigma_{\varepsilon_{j,1}}$ (see Table 1 and Subsection 3.B.1): total backscatter calibration at the calibration range ($R_{\mathrm{cal}} = R_{\max} = 6$ km). Error strength: $\pm 10\%$ Gaussian fluctuation over the nominal backscatter Rayleigh level at the calibration range. (a)–(b) Same descriptors as in Fig. 2.

identical to those in Fig. 3(b). In Figs. 4(c) and 4(d), spatially averaging $N = 25$ cells causes dramatic reduction of the backscatter error bars by about a factor $\sqrt{N} = 5$. Reference [30] also outlines (1) an "instantaneous noise effect" causing errors on the backscatter coefficient, which are proportional to the inverse of the SNR and (2) a "memory effect" including both (2a) the "cumulative effect from the inversion starting cell—i.e., the calibration cell—to the actual point at which the backscatter coefficient is evaluated" and (2b) "the effect of the noise in the resolution cell where the inversion is started." Compared with Table 1, it is clear that such reported "instantaneous noise effect" stands for the first term of Eq. (24) $[(\beta_j/U_j)^2\sigma_{U_j}^2]^{\frac{1}{2}} = \beta_j/\mathrm{SNR}_j$ [error source (iii)], and that the reported "memory effect" stands for the combined effect of $\sigma_{GU_j}^2$ in the second term of Eq. (24) [error source (iii)] with Eq. (26) [error source (iv)]. Historically, Knauss [32] (Eq. 14) also pinpointed the significance of the inverse SNR as an instantaneous noise effect.

B. Effects of Backscatter Calibration Error [Error Source (i), $\sigma_{\varepsilon_{j,1}}$ in Table 1, and Subsection 3.B.1; See Fig. 5]

Here, the nominal backscatter calibration at $R_{\mathrm{cal}} = R_{\max} = 6$ km (inside the molecular-atmosphere reference range, $R > 5$ km) $\beta_N = 1.1 \times 10^{-6}\ \mathrm{m}^{-1}\ \mathrm{sr}^{-1}$ is perturbed $\pm 10\%$, which simulates a user's relative error $\varepsilon_r^{\beta_N} = \sigma_{\beta_N}/\beta_N = 0.1$ (Gaussian distribution). Cross-examination of Figs. 5(b) and 3(b) evidences that the effects of a backscatter-calibration error are similar to those of noise corrupting the return power at the calibration cell. This can be reasoned by computing the ratio of error sources (i and iv) from Eqs. (13) and (26), respectively, as

$$\frac{\sigma_{\varepsilon_{j,1}}}{\sigma_{\varepsilon_{j,4}}} \approx \left|\frac{U_N}{\beta_N}\right| \frac{\sigma_{\beta_N}}{\sigma_{U_N}} = \mathrm{SNR}_{\mathrm{N}} \varepsilon_r^{\beta_N}, \tag{28}$$

where SNR_N stands for $\mathrm{SNR}(R_{\mathrm{cal}})$ in discrete notation. With $\mathrm{SNR}_N = 5$ and a user's calibration relative error, $\varepsilon_r^{\beta_N} = 0.1$, the backscatter error bar due to the

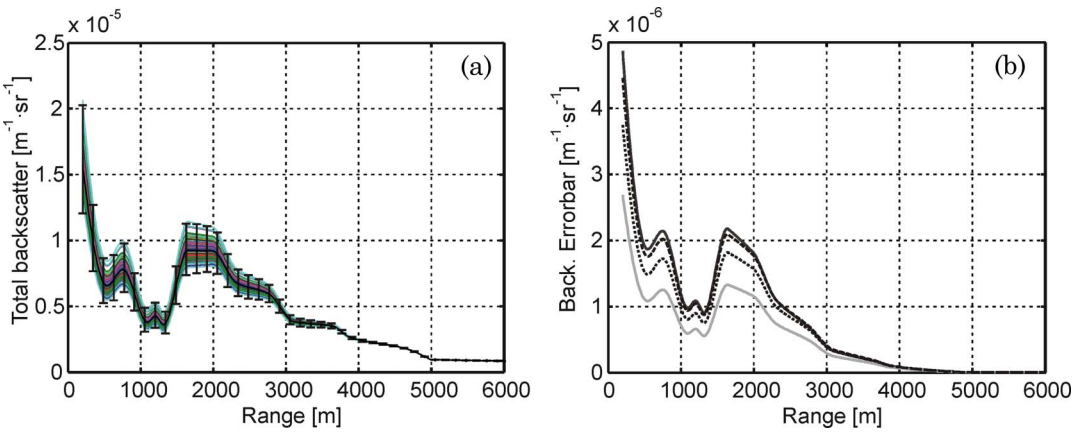

Fig. 6. (Color online) Error source (2), $\sigma_{\varepsilon_{j,2}}^{C}$ (see Table 1 and Subsection 3.B.2): Range-dependent lidar ratio, $S(R)$ (correlated errors). Error strength: 10% Gaussian fluctuation over the nominal total lidar ratio. (a)–(b) Same descriptors as in Fig. 2. In (b), analytical upper and lower error amplitudes are, respectively, plotted in dashed and dotted traces. MC upper and lower error amplitudes are plotted in a solid trace.

backscatter-calibration error is $\sigma_{\varepsilon_{j,1}} \approx 0.5\sigma_{\varepsilon_{j,4}}$, in accordance with Figs. 3(b) and 5(b).

C. Effects of Total Lidar-Ratio Errors [Error Source (ii), $\sigma_{\varepsilon_{j,2}}$ in Table 1 and Subsection 3.B.2; See Fig. 6]

As already introduced, the range-dependent total lidar ratio formulated in Eq. (27) above is used to replicate the two-component atmosphere of the present section, where we have constant lidar ratios for each type of scatterer (i.e., an aerosol lidar ratio $S^{\mathrm{aer}} = 50$ sr in the 0.2–5 km range and the well-known molecular ratio, $S^{\mathrm{mol}} = 8\pi/3$, over the whole inversion range). At 3.8 km the Rayleigh level is 50% of the aerosol level, and at 4.5 km it equals the aerosol level, so the atmospheric scene is aerosol-dominant up to approximately 4.5 km and molecular-dominant from 5 km onwards. Simulation conditions are $\mathrm{SNR}(R) \to \infty$ (all cells), perfect backscatter calibration, and 10% relative error in the total lidar ratio (correlated case, Subsection 3.B.2). The systematic relative error, p Eq. (14) is modeled as a Gaussian random variable with standard deviation $p = 0.1$.

Analytical backscatter error bars have been computed using second-order approximation Eq. (16), which in contrast to Subsections 4.A and 4.B now yields nonsymmetric upper and lower error amplitudes. Figure 6 shows that the analytical error bars give similar error levels to MC error bars but tend to slightly overestimate the lower error bar.

When lidar-ratio errors are assumed to be uncorrelated (a new simulation has been carried out with $\sigma_{S_k} = p_k S_k$, p_k independent Gaussian random variables with standard deviation $p_k = 0.1$; see Subsection 3.B.2), the error bars obtained are 1 order of magnitude lower than those for the correlated case [Fig. 6(b)] and with nearly identical shape. A suitable explanation for this is that lidar-ratio errors $S_k \pm dS_k$ tend to average out in Eq. (5) discrete integral, thus propagating lower error levels to the inverted backscatter than in the correlated case. As discussed in Subsection 3.B.2, the applicability of the uncorrelated case to stand-alone elastic lidar inversion (no cooperative Raman channel) is more theoretical than practical, being limited to an estimate of the lower error bound that would be obtained assuming random rather than systematic errors with range for the proposed lidar ratio.

D. Experimental Limits of Validity

Similar simulations been repeated for different atmospheric total optical depths ranging from very clear to thick atmospheres ($\tau = 0.1$ to 5) in order to assess approximate limits of validity of the analytical error bars derived (low optical depths for which application of the one-component algorithm is questionable have been included for numerical completeness). Upper and lower analytical error bars have been compared with the "true" MC counterparts in terms of the mean backscatter-relative error averaged over range and time, $\delta_r^{\beta}|_{u/l}$ (10^4 realizations in 100 MC sets of 100 inversions/set):

$$\delta_r^{\beta}|_{u/l} = \frac{1}{MN}\sum_{i=1}^{M}\sum_{j=1}^{N}\delta_{r,i}^{\beta_j}|_{u/l};$$
$$\delta_{r,i}^{\beta_j}|_{u/l} = \frac{\sigma_{\beta_j}^{A_i}|_{u/l} - \sigma_{\beta_j}^{MC_i}|_{u/l}}{\beta_j}, \tag{29}$$

where $\delta_{r,i}^{\beta_j}|_{u/l}$ is the backscatter-relative error for the ith set and range R_j, $\sigma_{\beta_j}^{A_i}$ and $\sigma_{\beta_j}^{\mathrm{MC}_i}$ are, respectively, the analytical and the MC backscatter error bars, u and l stand for upper and lower error bars, respectively, and M and N stand for the number of simulation sets and number of range cells, respectively.

The study has been parameterized for the two dominant error sources identified in Subsections 4.A–4.C above, the SNR at the maximum (calibration) range [error source (iv) in Table 1] and the relative error p [Eq. (14)] in the assumed total lidar ratio [error source (ii) in Table 1].

In the former case, the SNR at the minimum range, $\mathrm{SNR}(R_{\mathrm{min}})$ (equivalently, different lidar system emission energies or different telescope effective areas) has been tuned so as to ensure identical SNR at the maximum (calibration) range as above, $\mathrm{SNR}(R_{\mathrm{cal}}) = 5$ (a pessimistic value), and $\mathrm{SNR}(R_{\mathrm{cal}}) = 10$ (a more comfortable one). Although for the optically thick case $\tau = 5$ the simulation obviously requires an unrealistically high $\mathrm{SNR}(R_{\mathrm{min}})$, this case is numerically included as an asymptotic limit of the study. The mean and standard deviation of the estimated relative error on the upper and lower analytical error bars, $\delta_r^{\beta}|_u$ and $\delta_r^{\beta}|_l$, are shown in Table 2. Slight bias ($\delta_r^{\beta}|_u - \delta_r^{\beta}|_l$) arises in terms of underestimated upper error bars or overestimated lower error bars. This is especially the case in clear atmospheres and poor SNRs at the calibration range, $\mathrm{SNR}(R_{\mathrm{cal}}) = 5$, with errors on the predicted analytical error bars roughly between 15%–40% ($\tau = 5$ to 0.1, respectively), and below 10% for $\mathrm{SNR}(R_{\mathrm{cal}}) = 10$.

Table 2. Estimated Mean Relative Error and $1-\sigma$ Dispersion on Backscatter Analytical Error Bars for Different Optical Depths and Signal-to-Noise Ratios at Calibration Range [Error Source (ii) $\sigma_{\varepsilon_{j,4}}$, Only]

Optical Depth, τ	$\delta_r^{\beta}\|_{\mathrm{upper}}$ Eq. (29)	$\delta_r^{\beta}\|_{\mathrm{lower}}$
5	$-0.9 \pm 2.8(-14.0 \pm 14.0)\%$	$3.8 \pm 1.2(10.1 \pm 2.0)\%$
1	$-1.8 \pm 5.4(-20.2 \pm 21.4)\%$	$6.3 \pm 1.8(15.8 \pm 3.1)\%$
0.2	$-1.6 \pm 6.7(-28.8 \pm 30.0)\%$	$8.5 \pm 2.5(23.2 \pm 3.3)\%$
0.1	$-3.3 \pm 6.5(-39.5 \pm 31.4)\%$	$9.0 \pm 2.4(24.0 \pm 4.0)\%$

[a]Errors without/within brackets correspond to $\mathrm{SNR}(R_{\mathrm{cal}}) = 10$ and $\mathrm{SNR}(R_{\mathrm{cal}}) = 5$, respectively. Positive/negative mean values indicate error bar over/underestimation.

Table 3. Estimated Mean Relative Error and $1-\sigma$ Dispersion on Backscatter Analytical Error Bars for Different Optical Depths and Relative Error p in Assumed Total Lidar Ratio Eq. (14) [Error Source (ii) $\sigma_{\varepsilon_{j,2}}$, Only][a]

Optical Depth, τ	$\delta_r^\beta\|_{\text{upper}}$ Eq. (29)	$\delta_r^\beta\|_{\text{lower}}$
5	$0.1 \pm 4.8(-19 \pm 116) \times 10^3\%$	$4.0 \pm 1.7(-8 \pm 19) \times 10^3\%$
1	$0.9 \pm 2.0(-807 \pm 2462)\%$	$2.2 \pm 1.1(-626 \pm 1297)\%$
0.2	$0.5 \pm 0.5(-1.4 \pm 5.0)\%$	$0.7 \pm 0.4(4.0 \pm 1.5)\%$
0.1	$0.3 \pm 0.3(06 \pm 2.2)\%$	$0.4 \pm 0.3(2.2 \pm 1.2)\%$

[a]Errors without/within brackets correspond to $p = 0.1$ (10%) and $p = 0.5$ (50%), respectively. Underlined values correspond to divergent backscatter inversions (see text).

In the case of lidar-ratio errors (Table 3), the second-order analytical error bars are virtually identical to the "true" MC error bars for lidar-ratio errors of $\pm 10\%$ ($p = 0.1$) and optical depths $\tau \leq 5$ yielding mean backscatter-relative errors below approximately 4% and very low negative bias. In contrast to error source (iv), the error on the predicted analytical error bars increases with optically thicker atmospheres. For lidar-ratio errors about 50%, the quantitative validity of the analytical error bars is limited to $\tau < 1$ because for higher optical depths divergent inverted backscatter realizations occur, which pushes MC error bars to similar divergent figures. In spite of the fact that the analytical error bars fail to follow the MC error bars quantitatively, the analytical error bars exhibit similar divergent tendency and still contain most of the inverted noisy backscatter population, which is enough for most practical purposes.

5. Conclusions

A practical analytical error formulation to compute the total-backscatter error bars for the elastic one-component lidar inversion algorithm has been derived and validated with an MC method. The error source terms and computation procedure are summarized in Table 1.

It has been shown that the noise at the calibration cell [error source (iv)] plays a dominant role above the noise from all other range cells [30] [error source (iii)], and that error due to the backscatter calibration [error source (i)] can be analytically assimilated into the former error source (iv) via Eq. (28), thus leaving error sources (iv and ii) as the primary ones from an analytical point of view. Quantitatively, simulation results have shown that error sources (iv, i, and ii) can, however, yield comparable error levels for practical SNRs and typical user uncertainties in the algorithm inputs, which emphasizes the need of carefully considering these three errors sources in practical assessment of Klett's backscatter inversion error bars.

Experimental limits of validity of the analytical error bars have been derived in Tables 2 and 3 for primary error sources (iv, ii) in terms of the backscatter-relative error between the analytical and the MC error bars [Eq. (29)]. For optical depths $\tau \leq 5$ and $\mathrm{SNR}(R_{\mathrm{cal}}) = 10$, the estimated relative error is below 10%; for optical depths $\tau \leq 5$ and lidar-ratio errors of 10%, the estimated error is below approximately 4%.

The explicit error-propagated statistical formulation derived is—to the best of our knowledge—a complete treatment of the problem for practical SNRs in the state of the art of lidar inversion algorithms.

Appendix A: Derivation of Subsection 3.A Error Propagation Formulas

Hints are given on computation of error-propagation in Eqs. (8)–(11) from Eq. (7):

[Noise source (i)] error due to the backscatter calibration, $d\beta_N$ Eq. (8). Straightforward derivation from Eq. (4) and substitute the definition of β_j in the result obtained.

[Noise source (ii)] error due to the (range-dependent) lidar ratio, dS_k [Eq. (9)]. By using that $\frac{\partial \beta_j}{\partial S_k} = \frac{\partial \beta_j}{\partial G_j}\frac{\partial G_j}{\partial S_k}$ and, from Eq. (5), that

$$\frac{\partial G_j}{\partial S_k} = \begin{cases} 0 & k < j \\ w_k U_k & k \geq j \end{cases}, \tag{A1}$$

Equation (9) can be rewritten as

$$\varepsilon_{j,2} = \sum_{k=1}^{N} \frac{\partial \beta_j}{\partial S_k} dS_k = \frac{\partial \beta_j}{\partial G_j} \sum_{k=j}^{N} \frac{\partial G_j}{\partial S_k} dS_k. \tag{A2}$$

The term $\partial \beta_j / \partial G_j$ is computed from the modified KLT form of Eq. (4). After substituting Eq. (A1) into Eq. (A2) and collecting terms Eq. (4) again), Eq. (9) follows.

[Noise source (iii)] error due to the observation noise (range cells $1 \ldots N-1$), dU_k, $k = 1 \ldots N-1$. The mathematical steps involved parallel those carried out for the noise source (ii) above. Because the observation noise can be understood as a fluctuation of the power variable, P_j and, by definition, both the range-corrected power function, U_j, and G_j Eq. (3) depend on P_j, U_j, and G_j are introduced as auxiliary derivative variables as follows:

$$\begin{aligned} \varepsilon_{j,3} &= \sum_{k=1}^{N-1} \frac{\partial \beta_j}{\partial P_k} dP_k \\ &= \sum_{k=1}^{N-1} \left(\frac{\partial \beta_j}{\partial U_j}\frac{\partial U_j}{\partial P_k} + \frac{\partial \beta_j}{\partial G_j}\frac{\partial G_j}{\partial U_k}\frac{\partial U_k}{\partial P_k} \right) dP_k. \end{aligned} \tag{A3}$$

By using the range-corrected power definition Eq. (3), $U_j = R_j^2 P_j$, Eq. (A3) reduces to

$$\varepsilon_{j,3} = \frac{\partial \beta_j}{\partial U_j} dU_j + \frac{\partial \beta_j}{\partial G_j} \sum_{k=j}^{N} \frac{\partial G_j}{\partial U_k} dU_k. \tag{A4}$$

Following similar reasoning for the term $\partial G_j / \partial U_k$ [as in Eq. (A1)] and by computing the derivative terms above from Eqs. (3) and (4), the sought-after result of Eq. (10) yields:

[Noise source (iv)] error due to the observation noise at the calibration cell (range cell N), dU_N. $\varepsilon_{j,4}$ is computed as

$$\varepsilon_{j,4} = \frac{\partial \beta_j}{\partial P_N} dP_N = \frac{\partial \beta_j}{\partial U_N} dU_N + \frac{\partial \beta_j}{\partial G_j} \frac{\partial G_j}{\partial U_N} dU_N, \tag{A5}$$

where

$$\frac{\partial G_j}{\partial U_N} = \begin{cases} w_N S_N & j < N \\ 0 & j = N \end{cases}. \tag{A6}$$

Using Eqs. (3) and (A6) above, Eq. (11) is reencountered.

Appendix B: Error Due to Correlated Total Lidar-Ratio Errors

For this error source, the lidar ratio is assumed to be known with a systematic relative error, $\pm p$. Thus, the inverted backscatter [Eq. (4)] given a user-defined lidar ratio, $S_{\text{user}}(R) = S(R)(1+p)$, takes the form

$$\beta_j(\beta_N, \vec{S}, \vec{U}) = \frac{\beta_N U_j}{U_N + 2\beta_N (1+p) G_j(\vec{S}, \vec{U})}, \tag{B1}$$

where it has been used that $G_j[(1+p)\vec{S}, \vec{U}] = (1+p) G_j[\vec{S}, \vec{U}]$ after Eq. (5). From Eq. (B1) above, the backscatter error due to a relative error on the lidar ratio, p, is computed using a second-order series expansion as

$$\begin{aligned} |\Delta \beta_j(p)| &= |\beta_j(p) - \beta_j(p=0)| \\ &\approx \left| \frac{\partial \beta_j}{\partial p}\bigg|_{p=0} p + \frac{1}{2} \frac{\partial^2 \beta_j}{\partial p^2}\bigg|_{p=0} p^2 \right|, \end{aligned} \tag{B2}$$

where

$$\frac{\partial \beta_j}{\partial p}|_{p=0} = -\frac{2\beta_j^2}{U_j} G_j,$$

$$\frac{\partial^2 \beta_j}{\partial p^2}|_{p=0} = \frac{8\beta_j^3}{U_j^2} G_j^2.$$

If p is considered the relative error on the total lidar ratio at the $1-\sigma$ level, then $|\Delta \beta_j|$ represents the expected $1-\sigma$ error bar contribution and Eq. (B2) reencounters Eq. (16) in Subsection 3.B.

The authors wish to acknowledge the European Commission under the EARLINET-ASOS (European Aerosol Research Lidar Network–Advanced Sustainable Observation System) (European Union Coordination Action) contract RICA-025991, and European Union Specific Support Action contract 011863 (RIDS), the European Space Agency under contract 21487/08/NL/HE, the Spanish Ministry of Science and Innovation and FEDER (European Regional Development) funds under the projects TEC2009-09106 and Complementary Actions CGL2009-08031-E/CLI ("Charmex"), CGL2008-01330-E/CLI, and CTM2006-27154-E. The Generalitat de Catalunya/AGAUR (Agency for Management of University and Research Grants) is also thanked for Md. Reba's predoctoral fellowship.

References

1. J. A. Reagan, X. Wang, and M. T. Osborn, "Spaceborne lidar calibration from cirrus and molecular backscatter returns," IEEE Trans. Geosci. Remote Sensing **40**, 2285–2290 (2002).
2. D. Winker, J. Pelon, and M. McCormick, "Initial results from CALIPSO," in *Reviewed and Revised Papers Presented at the 23rd International Laser Radar Conference*, C. Nagasawa and N. Sugimoto, eds. (IOP, 2006), pp. 991–994.
3. H. Nett and M. Endemann, "Atmospheric Dynamics Mission: AEOLUS," *Proceedings of the IEEE International Geoscience and Remote Sensing Symposium* (IEEE, 2004), Vol. 2, pp. 1190–1195.
4. European Space Agency's Wind Mission ADM-AEOLUS, Tech. Rep. BR-236 (European Space Research and Technology Centre, 2005).
5. C. Böckmann, D. Müller, L. Osterloh, P. Pornsawad, and A. Papayannis, "From EARLINET-ASOS Raman-Lidar signals to microphysical aerosol properties via advances regularizing software," in *Proceedings of the IEEE International Geoscience and Remote Sensing Symposium* (IEEE, 2008), pp. (II-422)–(II-425).
6. W. Hitschfeld and J. Bordan, "Errors inherent in the radar measurement of rainfall at attenuating wavelengths," J. Appl. Meteorol. **11** 58–67 (1954).
7. E. W. Barrett and O. Ben-Dov, "Application of the lidar to air pollution measurements," J. Appl. Meteorol. **6** 500–515 (1967).
8. W. Viezee, E. E. Uthe, and R. T. H. Collis, "Lidar observations of airfield approach conditions: an exploration study," J. Appl. Meteorol. **8**, 274–283 (1969).
9. P. A. Davis, "The analysis of lidar signatures of cirrus clouds," Appl. Opt. **8**, 2099–2102 (1969).
10. F. G. Fernald, B. M. Herman, and J. A. Reagan, "Determination of aerosol height distribution by lidar," J. Appl. Meteorol. **11** 482–489 (1972).
11. R. T. H. Collis and P. B. Russell, "Lidar measurement of particles and gases by elastic backscattering and differential absorption," in *Laser Monitoring of the Atmosphere*, E. D. Hinkley, ed. (Springer-Verlag, 1976), pp. 71–102.
12. R. H. Kohl, "Discussion of the interpretation problem encountered in single-wavelength lidar transmissometers," J. Appl. Meteorol. **17**, 1034–1038 (1978).
13. J. D. Klett, "Stable analytical inversion solution for processing lidar returns," Appl. Opt. **20**, 211–220 (1981).
14. F. G. Fernald, "Analysis of atmospheric lidar observations: some comments," Appl. Opt. **23**, 652–653 (1984).
15. Y. Sasano, E. V. Browell, and S. Ismail, "Error caused by using a constant extinction/backscattering ratio in the lidar solution," Appl. Opt. **24**, 3929–3932 (1985).
16. J. D. Klett, "Lidar inversion with variable backscatter/extinction ratios," Appl. Opt. **24**, 1638–1643 (1985).

17. World Meteorological Organization Global Atmosphere Watch, "Plan for the implementation of the GAW Aerosol Lidar Observation Network (GALION)," TD 1443 (World Meteorological Organization, 2007).
18. J. D. Klett, "Lidar calibration and extinction coefficients," Appl. Opt. **22**, 514–515 (1983).
19. J. D. Klett, "Extinction boundary value algorithms for lidar inversion," Appl. Opt. **25**, 2462–2464 (1986).
20. A. Ansmann, U. Wandinger, M. Riebesell, C. Weitkamp, and W. Michaelis, "Independent measurement of extinction and backscatter profiles in cirrus clouds by using a combined Raman elastic-backscatter lidar," Appl. Opt. **31**, 7113–7131 (1992).
21. M. Sicard, P. Chazette, J. Pelon, J. Gwang-Won, and Soon-Chang Yoon, "Variational method for the retrieval of the optical thickness and the backscatter coefficient from multiangle lidar profiles," Appl. Opt. **41**, 493–502 (2002).
22. G. J. Kunz, "Transmission as an input boundary value for an analytical solution of a single-scatter lidar equation," Appl. Opt. **35**, 3255–3260 (1996).
23. V. A. Kovalev, "Lidar measurement of the vertical aerosol extinction profiles with range-dependent backscatter-to-extinction ratios," Appl. Opt. **32**, 6053–6065 (1993).
24. V. A. Kovalev, "Stable near-end solution of the lidar equation for clear atmospheres," Appl. Opt. **42**, 585–591 (2003).
25. L. R. Bissonnette, "Sensitivity analysis of lidar inversion algorithms," Appl. Opt. **25**, 2122–2125 (1986).
26. F. Rocadenbosch and A. Comerón, "Error analysis for the lidar backward inversion algorithm," Appl. Opt. **38**, 4461–4474 (1999).
27. J. Qiu, "Sensitivity of lidar equation solution to boundary values and determination of the values," Adv. Atmos. Sci. **5**, 229–241 (1988).
28. M. Matsumoto and N. Takeuchi, "Effects of misestimated far-end boundary values on two common lidar inversion solutions," Appl. Opt. **33**, 6451–6456 (1994).
29. F. Rocadenbosch, A. Comerón, and D. Pineda, "Assessment of lidar inversion errors for homogeneous atmospheres," Appl. Opt. **37**, 2199–2206 (1998).
30. A. Comerón, F. Rocadenbosch, M. A. López, A. Rodríguez, C. Muñoz, D. García-Vizcaíno, and M. Sicard, "Effects of noise on lidar data inversion with the backward algorithm," Appl. Opt. **43**, 2572–2577 (2004).
31. M. Sicard, A. Comerón, F. Rocadenbosch, A. Rodríguez, and C. Muñoz, "Quasi-analytical determination of noise-induced error limits in lidar retrieval of aerosol backscatter coefficient by the elastic, two-component algorithm," Appl. Opt. **48**, 176–182 (2009).
32. D. C. Knauss, "Significance of the boundary value term in the Klett lidar inversion formula," Appl. Opt. **21**, 4194–4194 (1982).
33. H. G. Hughes, J. A. Ferguson, and D. H. Stephans, "Sensitivity of a lidar inversion algorithm to parameters relating atmospheric backscatter and extinction," Appl. Opt. **24**, 1609–1613 (1985).
34. M. Keastner, "Lidar inversion with variable backscatter/extinction: comment," Appl. Opt. **25**, 833–835 (1986).
35. Y. S. Balin, S. I. Kavkyanov, G. M. Krekov, and I. A. Razenkov, "Noise-proof inversion of lidar equation," Opt. Lett. **12**, 13–15 (1987).
36. J. D. Spinhirne, J. A. Reagan, and B. M. Herman, "Vertical distribution of aerosol extinction cross section and interference of aerosol imaginary index in the troposphere by lidar technique," J. Appl. Meteorol. **19**, 426–438 (1980).
37. R. J. Barlow, "Theoretical distributions," in *Statistics. A Guide to the Use of Statistical Methods in Physical Sciences* (Wiley, 1999), pp. 28–33.
38. M. N. Md. Reba, F. Rocadenbosch, and M. Sicard, "A straightforward signal-to-noise ratio estimator for elastic/Raman lidar signals," Proc. SPIE **6362**, 636223 (2006).
39. B. A. Bodhaine, N. B. Wood, E. G. Dutton, and J. R. Slusser, "On Rayleigh optical depth calculations," J. Atmos. Ocean. Technol. **16**, 1854–1861 (1999).